Extratropical Transition and Re-Intensification of Typhoon Toraji (2001): Large-Scale Circulations, Structural Characteristics, and Mechanism Analysis

ZHU Xiande[1], WU Lixin[1], [*], and WANG Qi[2]

1) *Physical Oceanography Laboratory, Ocean University of China, Qingdao* 266100, *China*
2) *College of Oceanic and Atmospheric Sciences, Ocean University of China, Qingdao* 266100, *China*

Abstract With the use of data from the National Centers for Environmental Prediction Climate Forecast System Reanalysis, the environment and structure of typhoon Toraji (2001) are investigated during the re-intensification (RI) stage of its extratropical transition (ET), a process in which a tropical cyclone transforms into an extratropical or mid-latitude cyclone. The results provide detailed insight into the ET system and identify the specific features of the system, including wind field, a cold and dry intrusion, and a frontal structure in the RI stage. The irrotational wind provides the values of upper- and lower-level jets within the transitioning tropical cyclone and the cyclone over Shandong Peninsula, accompanied with the reduced radius of maximum surface winds around the cyclone center in the lower troposphere. Simultaneously, dry air intrusion enhances the formation of fronts and leads to strong potential instability in the southwest and northeast quadrants. The distribution of frontogenesis shows that the tilting term associated with vertical motion dominates the positive frontogenesis surrounding the cyclone center, especially in the RI stage. The diagnostics of the kinetic energy budget suggest that the divergent kinetic energy generation whose time evolution corresponds well to that of cyclone center pressure is the primary factor for the development of Toraji in the lower troposphere. The ET of Toraji is a compound pattern that contains a development similar to that of a B-type extratropical cyclone within the maintaining phase and an A-type extratropical cyclone within the strengthening period, which corresponds to the distribution of the E-P fluxes with vertically downward propagation in the maintaining stage and upwards momentum in the strengthening phase.

Key words typhoon Toraji; extratropical transition; re-intensification; upper level jet; frontogenesis; energy budget

1 Introduction

Extratropical transition (ET) of tropical cyclones (TCs) is a process in which a TC transforms into an extratropical (or mid-latitude) cyclone (Evans and Hart, 2008). This process can be generally considered a transformation from a symmetric warm-core TC to an asymmetric cold-core cyclone (Quinting *et al.*, 2014). Approximately 45% of TCs interact with mid-latitude flow after recurvature (Jones *et al.*, 2003) and undergo ET, with more than 50% of these storms re-intensifying as extratropical cyclones (ECs) in the North Atlantic basin (Hart and Evans, 2001). Klein *et al.* (2000) developed a three-dimensional conceptual model of ET, in which the process of ET is split into the two following stages: extratropical transformation and re-intensification (RI).

ET and RI always produce intense rainfall, which results in catastrophic inland flooding (DiMego and Bosart, 1982a, b), damaging winds (Merrill, 1993; Evans and Hart,

2008), and marine hazard (Sekioka, 1956a; Sinclair, 2002). Thus, the ET of TC has been studied through numerous research cases (Sekioka, 1956a, b; DiMego and Bosart, 1982a, b; Evans and Prater-Mayes, 2004; Kitabatake, 2008; Harr and Dea, 2009; Chen and Pan, 2010; Cordeira and Bosart, 2011) and climatologies (Harr and Elsberry, 2000; Klein *et al.*, 2000, 2002; Hart and Evans, 2001; Jones *et al.*, 2003; Dare and Davidson, 2004), which indicate the evolution of features and characteristics of ET. At the transformation stage, the characteristics of the interaction between the cyclone and the mid-latitude systems include asymmetric wind, thermal structure, moisture, precipitation, cloud, and convection (Sekioka, 1970; Jones *et al.*, 2003), and the dispersal of the upper-level TC warm core (Ritchie and Elsberry, 2001). The RI stage is identified by the deepening of the EC with frontogenesis and asymmetric wind, cloud, and precipitation patterns (Harr and Hogan, 2000). Some results of ET research (DiMego and Bosart, 1982a, b; Foley and Hanstrum, 1994; Harr and Elsberry, 2000; Harr and Hogan, 2000) show that the RI of TC is similar to the development of a B-type EC (Petterssen and Smebye, 1971), which occurs when a strong upper trough

---

* Corresponding author. E-mail: lxwu@ouc.edu.cn

is moving over a low-level warm advection (The B-type EC occurs when a strong upper trough is moving over a low-level warm advection. In this process, the cyclone enhances because of the strong vorticity advection from the upper level. The A-type EC is similar to the cyclone inspired by the frontal wave, which is relevant to baroclinic instability with strong temperature advection in the lower atmosphere).

Previous studies show that the transition of TC is closely related to cold air intrusion (Chen, 2000; Zhu *et al.*, 2005b). During the interaction of the TC and the mid-latitude baroclinic zone, the cold air moves west and warm air moves east (Vancas, 2006). Cold air intrusion can aggravate deep convection when the cold air meets warm and moist air from TCs (Emanuel *et al.*, 1994). Simultaneously, a front is always formed. At the transformation stage, warm frontogenesis arises in the northeast quadrant of the TC in transition because of the modification of the equivalent potential temperature gradient, and cold frontogenesis to the west of the TCs is suppressed because of thermally directed circulation (Harr and Elsberry, 2000).

The westerly belt plays an important role in ET (Dimego and Bosart, 1982a, b; Harr and Elsberry, 2000; Harr and Hogan, 2000). Klein *et al.* (2002) numerically investigated the ET and RI of the occurrence of TC in the northwest Pacific Ocean and found a complex dynamical interaction between the westerly belt and the cyclones in transition. The upper jet persists because of the release of the latent heat of the cyclone (Palmen, 1958). Bosart and Atallah (2000) and McTaggart-Cowan (2002) pointed out that the relative position between the cyclone in transition and the jet is important.

In this paper, we study the evolution of Toraji (2001), which contains ET and RI in a baroclinic environment. Toraji remained for a long time and brought catastrophic inland flooding and strong winds after landfall, which resulted in significant financial damage. Some previous studies (Han *et al.*, 2005; Li *et al.*, 2004) showed the structure of typhoon Toraji in the synoptic situation and frontogenesis, and concluded some reasons for the RI. However, the analysis of the RI mechanism process of Toraji is insufficient and unsystematic. Thus, this case needs to be studied to improve TC forecasting and reduce hazardous damage.

This paper is organized as follows: Section 2 presents the data and the methodology. Section 3 contains the overview of typhoon Toraji and the synoptic situation during the ET. Section 4 focuses on the synoptic situation and structural characteristics during the RI period with some possible mechanisms for the observed structure. Section 5 presents the conclusions and discussions.

2 Dataset and Methods

The best track data from the Japan Meteorological Agency (JMA, http://agora.ex.nii.ac.jp/digital-typhoon/index.html.en) show that typhoon Toraji formed near the Philippines as a tropical depression and then moved northwestward.

To investigate the structure of the ET and RI of the system, we used the reanalysis dataset of the National Center for Atmospheric Research (NCAR) archived at the National Centers for Environmental Prediction (NCEP) Climate Forecast System Reanalysis (CFSR) data, with a 0.5°×0.5° horizontal resolution at 6h intervals. The 25-year Reanalysis Project (JRA-25) data with 1.25°×1.25° resolution from Japan Meteorological Agency (JMA (Onogi *et al.*, 2007) are compared with CFSR data. The results of the two datasets are similar in terms of the ET evolution. The CFSR data are adopted in this paper because of their finer grid. The Multi-Functional Transport Satellite (MT-SAT)-1R images of Geostationary Operational Environmental Satellite (GOES-9) were used for assistant analysis.

3 Overview of Typhoon Toraji

Toraji originated from a tropical disturbance east of the Philippines (Fig.1a) at 0000 UTC July 25, 2001. TC Toraji first attained tropical storm intensity on July 27 when it was moving northwestward with the maximum surface wind (MSW) exceeding 34 kt (kt, knots per hour, 1 kt = 0.514 m s^{-1}) (Fig.1b). The storm intensified slowly in the following 18 h. The system was labeled a typhoon by the Joint Typhoon Warning Center; at that time, the wind speed was 65 kt. Twelve hours later at 0600 UTC 28 July, it peaked in intensity, the minimum sea level pressure (MSLP) was 960 hPa, and the MSW speed was 75 kt. This TC maintained its peak intensity for approximately 30 h. Toraji's track shifted northward and its intensity decreased because of the topography when it made landfall in Taiwan at 1500 UTC 29 July and then became a severe tropical storm 3 h later. As the storm decayed, the symmetrical structure disappeared, and the storm weakened into a tropical depression before and after it made landfall in Zhejiang because of the enhanced friction and reduction of moisture supplies. Subsequently, Toraji moved northward and was back over the ocean, where it evolved to an EC and intensified. Finally, the system weakened over the Bohai Sea and dissipated. The RI stage of Toraji is the major objective in this study, which is highlighted in Fig.1a. The research time is noted as extratropical transition cyclone (ETC) in this paper.

The asymmetric characteristic of the cloud structure when the typhoon made landfall at Zhejiang (Fig.2a) indicated that the cyclone was at the transformation stage of ET (Klein *et al.*, 2000). The cloud around ETC exhibited the features of a stratus cloud. Images showed a hollow configuration and the comma structure of the spiral cloud band and intense convection in the outer edge of the northeast quadrant due to RI of the cyclone (Figs.2c–2d). At the same time, the satellite infrared images (not shown) demonstrated that a convective cloud developed in the northeastern side of the cyclone. Furthermore, infrared and water vapor satellite images (not shown) indicated a tongue of cold dry air invading from northwest to southwest around the center of Toraji.
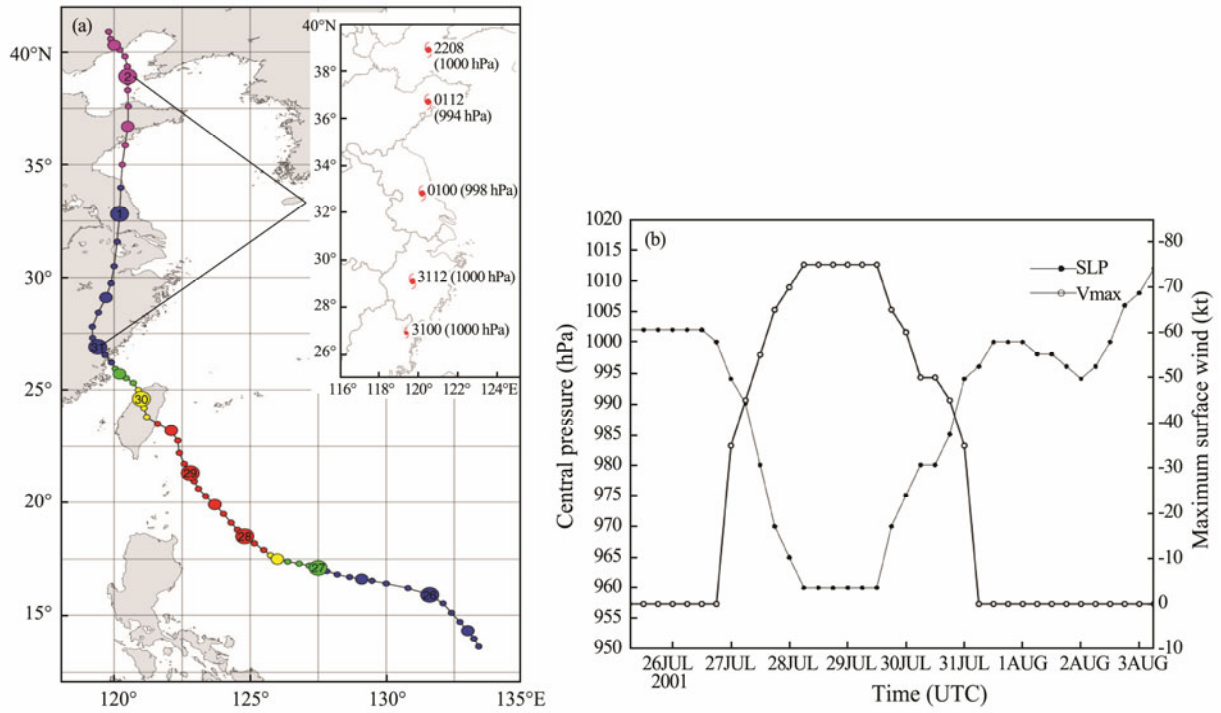
Fig.1 (a) Track of TC Toraji from JMA (http://agora.ex.nii.ac.jp/). Circles are placed every 6 h. (Blue, tropical depressions; Green, tropical storm; Yellow, severe tropical storm; Red, typhoon; Pink, extratropical cyclone). (b) Time series of best-track central pressure (SLP; solid lines with dots; hPa) and maximum sustained wind speed (Vmax; solid lines with circles; kt). The little figure in (a) is the research stage.
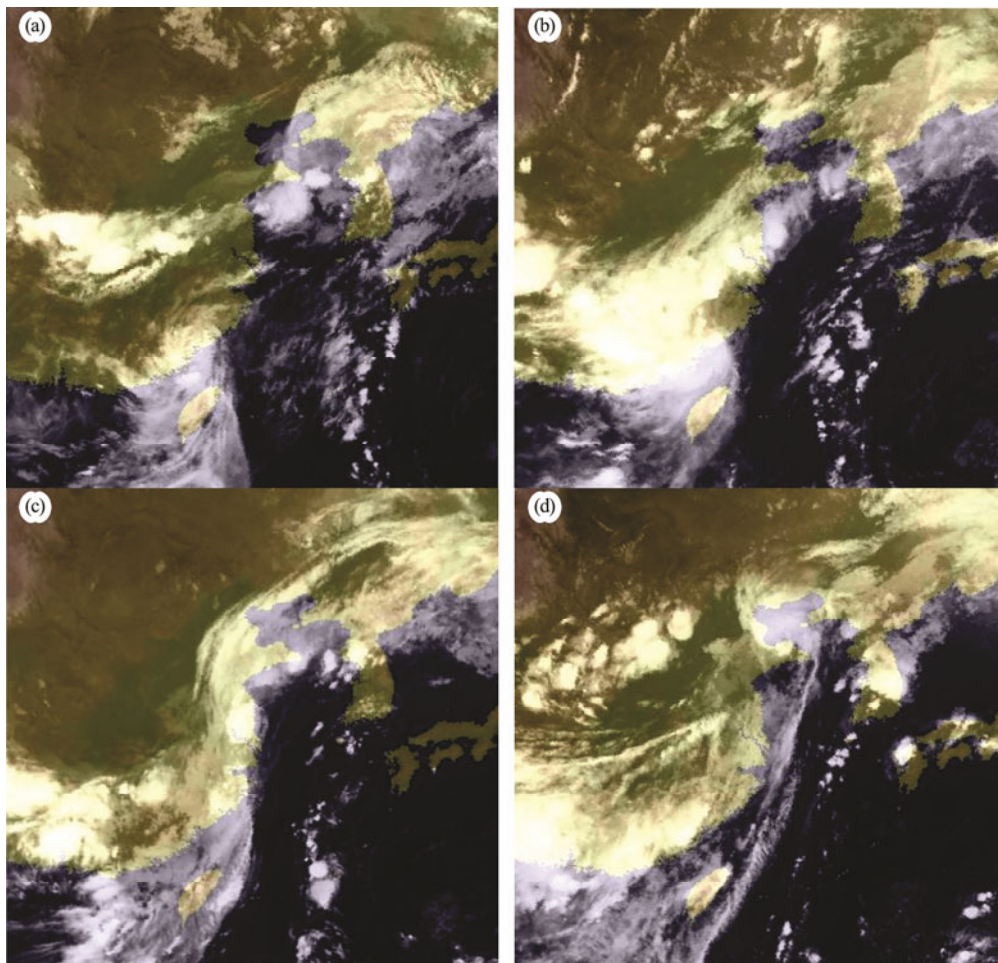
Fig.2 MTSAT-1R1 images at (a) 0000 UTC 31 Jul, (b) 1200 UTC 31 Jul, (c) 0000 UTC 01 Aug, and (d) 1200 UTC 01 Aug.

4 Synoptic and Structure Characteristics

4.1 Synoptic Situation

Fig.3 show the 500 hPa geopotential height field associated with Toraji. The cyclone decayed to the bottom with a minimum central pressure of 1000 hPa and a pattern with a closed 500 hPa geopotential height contour at 0000 UTC 31 July (Fig.3a). After 12 h (Fig.3b), the outermost closed contour of the 500 hPa geopotential height fields of the cyclone became open (OW structure, contoured every 20 m) and evolved to a weak trough, which indicated the end of the transformation stage (Klein *et al.*, 2000). At this stage, the storm presented the features of a baroclinic cyclone, and cold air invaded the storm. Such time is potentially defined as the ET completion time by Demirci *et al.* (2007). At the transformation stage, a trough (TR1) was located northwest of the storm, and a following ridge (RD) was noted at 500 hPa along 100°E on 31 July. As Toraji moved northward, it began to merge with TR1, and the ETC developed (Fig.3c). At the same time, TR1 expanded equatorward and evolved into a cyclone with a closed contour of the 500-hPa geopotential height fields (5780 m) and another trough (TR2) formed on the north of TR1. The center of the ETC was located to the northeast of TR1 when the intensity of Toraji peaked again,

and TR1 separated from the original low system (Fig.3d). At this RI stage, the gradient of geopotential heights between TR1 and the subtropical anticyclone increased. Simultaneously, RD extended eastward to the subtropical high over the West Pacific Ocean and cut off the joint of TR1 and the north low system along 42°N. The above discussion shows that the upflow before a strong trough and the increased gradient of geopotential heights provided favorable conditions for the TC (Petterssen and Smebye, 1971).

The wind field at 850 hPa (Fig.3) exhibited an asymmetrical pattern with strong wind in the southeast and northeast quadrants of ETC, and a weak wind on the left side of the motion direction before ET completion (Figs. 3a–3b), which is consistent with the results of Jones *et al.* (2003) and Quinting *et al.* (2014). Simultaneously, ETC entered the left area of the low-level jet (LJ), where the existence of upflow further provoked convective development. At the RI stage (Figs.3b–3d), closed circulation of the wind field around the center was formed again when Toraji moved northward along the left-hand of LJ and joined another closed cyclonic circulation (shown in Figs.3a and 3b) over Shandong Peninsula. Meanwhile, a new expansion of the storm-forced wind gradually emerged in the northwest quadrant close to the best track center.

Fig.3 shows the distributions of θ at 850-hPa during ET
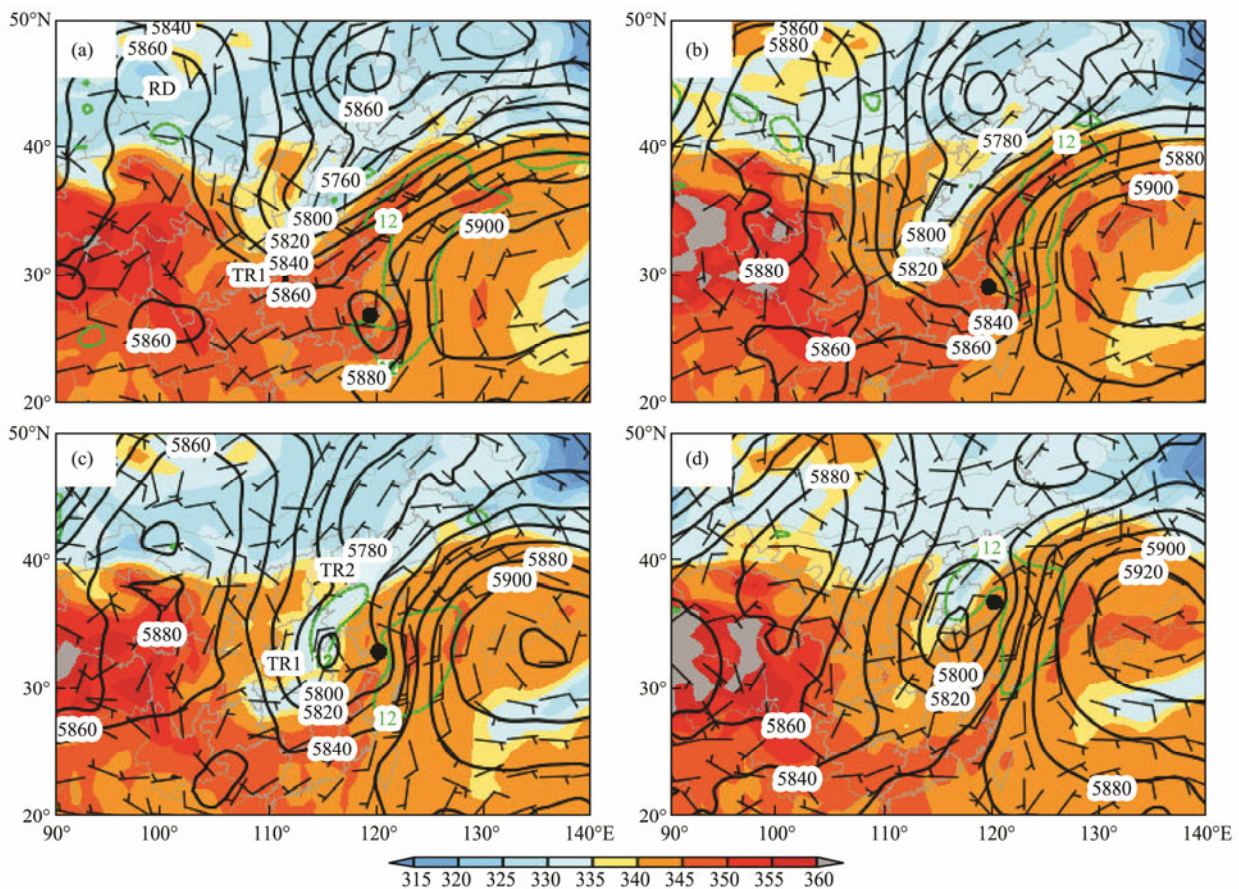
Fig.3 Geopotential height (gpm; solid lines) at 500 hPa, potential temperature (θ, K; shaded), wind (m s⁻¹; barbs, with a full line representing 10 m s⁻¹), and low-LJ stream (winds in the region surrounded by the green dashed lines are greater than 12 m s⁻¹) at 850 hPa at (a) 0000 UTC 31 Jul, (b) 1200 UTC 31 Jul, (c) 0000 UTC 01 Aug, (d) 1200 UTC 01 Aug. (●: the location of typhoon center).

and RI. At 0000 UTC 31 July, Toraji evolved into a baroclinic cyclone, and a cold tongue corresponding with TR1 was observed to the northwest of the ETC. The cold air intrusion resulted in increased temperature gradient in the northwest of the warm core cyclone (Fig.3a). Afterwards, the cold tongue extended southward by advection, and the ETC intensified (Figs.3b–3d). During this period, the temperature gradient increased northwest of the cyclone while the typhoon was moving northward. The intrusion of cold air can induce tilt and aggravate the vertical shear of a TC in its extratropical transformation (Jones, 1995; Jones *et al.*, 2003), and enhance the baroclinic instability, which precipitates the conversion from baroclinic energy to kinetic energy (Chen and Ding, 1979).

The pumping of high-altitude divergence enhanced vertical motion when the ETC moved to the upper-level jet (ULJ) entrance area during RI (Fig.4) with opposite circulations in the both sides of the entrance region. At the RI stage, TR1 helped enhance the irrotational outflow associated with the ETC (Figs.4a–4c), which indicates an increasing interaction between the ETC and the subtropical trough (TR1). The component of the irrotational outflow perpendicular to the axis of the ULJ increased to a local maximum of $18\,\mathrm{m\,s^{-1}}$ at 0000 UTC 1 August (Fig.4c). Simultaneously, the western portion of the outflow from Toraji also helped strengthen the trough (TR1). Subsequently, the ETC center was coincident with the center of the irrotational outflow when ETC intensified to its peak again (Fig.4d). The distribution of PV in Fig.4 showed that PV was characterized by a strong positive anomaly associated with TR1, TR2, and the ULJ with values exceeding 6 potential vorticity units (PVU) (1 PVU=1×10^{-6} $\mathrm{K\,kg^{-1}\,m^2\,s^{-1}}$). The PV gradient on the northwestern edge of the ULJ increased, which in turn contributed to the intensification of Toraji *via* downward-conveyor momentum. The relative position between the TC and upper jet is important, as shown in previous research (McTaggart-Cown, 2002).
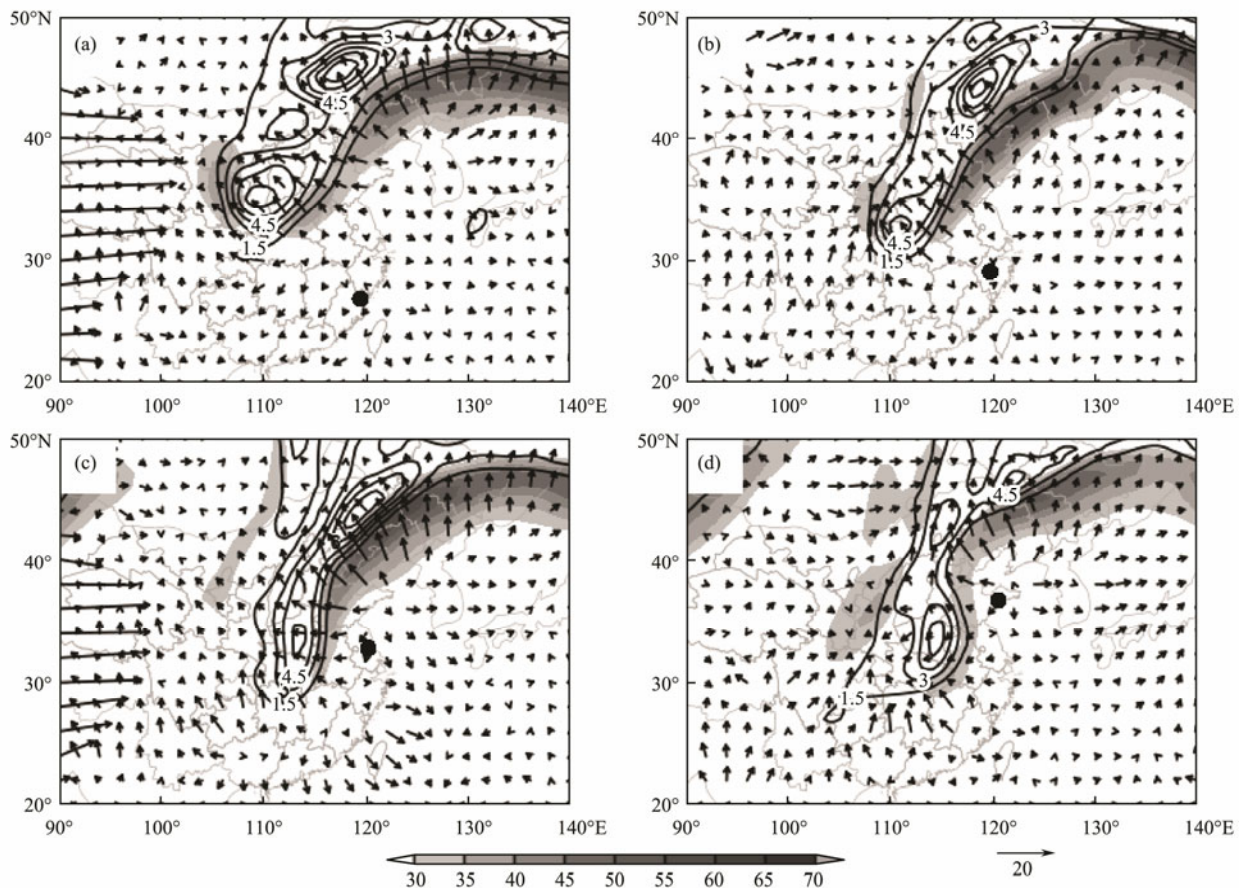
Fig.4 Total wind magnitude (shaded, beginning 30; $\mathrm{m\,s^{-1}}$), PV (contours; PVU), and irrotational wind (arrows; $\mathrm{m\,s^{-1}}$) at 250-hPa at (a) 0000 UTC 31 Jul, (b) 1200 UTC 31 Jul, (c) 0000 UTC 01 Aug, (d) 1200 UTC 01 Aug. (●: the location of typhoon center).

4.2 Structure Characteristics

As shown in Fig.3, the circulation of ETC center was open with minimum wind in the left-hand side of the best track at 850 hPa. Fig.5a depicts the evolution of the 10 m wind field parallel to the best track throughout the end of transformation and the entire RI stage. The asymmetrical structure was obvious, with the maximum wind observed to the right of the cyclone before the development of the system. At the RI stage, the wind field exhibited strong wind on both sides of the moving ETC with the magnitude of the wind reinforcing on the left side, which is

similar to the 'left-hand side contribution' (Loridan *et al.*, 2014). Meanwhile, the radius of MSW shrank inwardly again on both sides of the ETC at 0000 UTC 1 August. An inward displacement of the from approximately 2 to 3 degrees of longitude or latitude was noted in conjunction with the acceleration of approximately $11\,\mathrm{m\,s^{-1}}$ of the wind field on both sides at 1600 UTC 1 August. Nevertheless,

the asymmetrical phenomenon existed through the ET period at 500 hPa (Fig.5b). The time when the maximum wind reached 500 hPa was 6 h earlier than that near the surface (Fig.5a) on the right side of the ETC. At the RI stage, positive wind (southward) replaced negative wind (northward) over the storm center, which demonstrated the enhanced baroclinic cyclone.
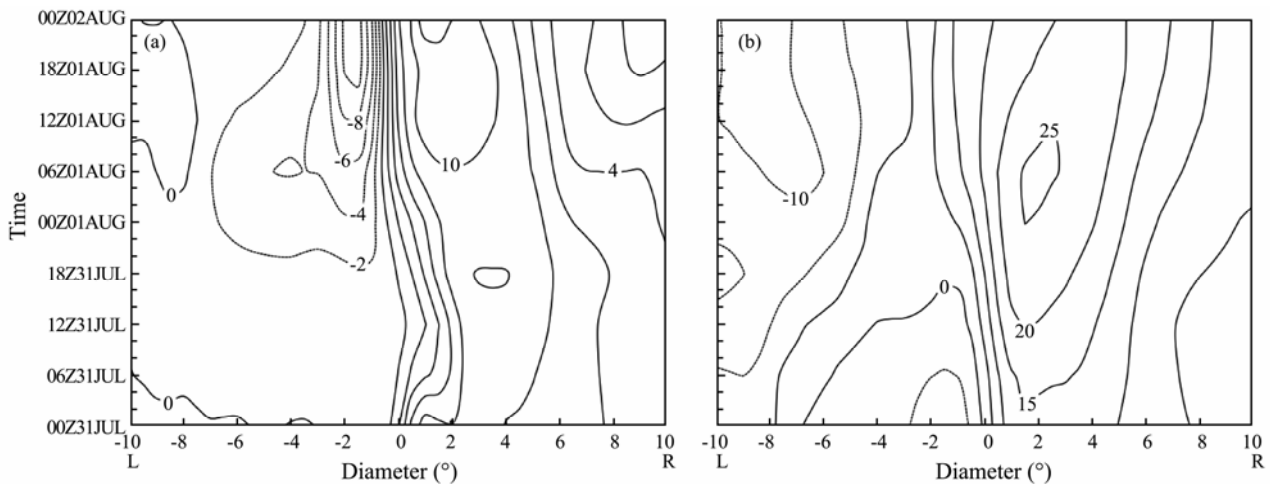
Fig.5 (a) 10 m wind field parallel to the best track representing the tangential wind speeds ($\mathrm{m\,s^{-1}}$). (b) as in (a), but at 500 hPa. Positive wind speed corresponds to the moving direction of the typhoon. (L: left; R: right. 0: the location of typhoon center).

The features of the surface latent heat flux (SLHF), the 950 hPa wind field, and PV are shown in Fig.6. The circulation of the non-divergent (Fig.6a) wind field exhibited an asymmetrical pattern in the north–south direction with strong wind over the sea and weak wind over land when the storm made landfall in Zhejiang Province, which is similar to the evolution of the 10 m wind field (Fig.5a). The irrotational wind field showed a strong inflow of approximately $10\,\mathrm{m\,s^{-1}}$ on the east side of the storm (Fig.6b). By contrast, the distribution of θ surrounding the system showed a warm core at a low-level atmosphere with a warm area on the left-hand of the best track. A wider band of weaker PV occurred at the center (Fig.6b), and preexisting PV was broken in the south of the ETC (not shown). At the same time, SLHF exhibited a strong band starting on the northwest side of the ETC and extending around the west to the southwest side (Fig.6a), where the convective cloud developed (Fig.2b). At the RI stage, the circulation of non-divergent wind developed quasi-symmetrically with a speed exceeding $18\,\mathrm{m\,s^{-1}}$ surrounding the ETC center (Fig.6c). Correspondingly, the irrotational wind was characterized by another asymmetry with the strong and weak inflow on the western and eastern side of the ETC, respectively (Fig.6d). The inflow on the west side associated with enhanced PV (Fig.6d) was much stronger than that at 0600 UTC 31 July. Simultaneously, the equivalent potential temperature gradient strengthened in the northeast–southwest direction near the center because of cold air intrusion. Afterwards, the cold air extended from the western side to the southern side of the center by advection, and the ETC intensified with the increased inflow surrounding ETC at 1200 UTC 1 August

(not shown). During the development period, a reduced SLHF was located at the inner core of Toraji, although the θ gradient increased at that location. Interestingly, the SLHF increased in the northeast and southwest quadrant of the ETC, but the distance from the center increased (Fig.6c). The result revealed that the influence of moist static energy to the outward convection shifted, which corresponded to the 'hollow configuration' cloud (Fig.2d). The release of latent heat was favorable to the strong contrast of cool and warm air masses across a frontal zone and the incitation of cloud (Wang *et al.*, 2002).

Fig.7 shows the vertical structure change of radial wind and tangential winds at different times. At 0600 UTC 31 July, the radial wind showed a strong inflow below 500 hPa on the southern side of the ETC, with a maximum speed greater than $9\,\mathrm{m\,s^{-1}}$ at 750 hPa (Fig.7a). The inflow almost covered the southern side of Toraji from near 26.2°N. Meanwhile, the outflow was approximately 450 hPa, with a maximum speed reaching $3\,\mathrm{m\,s^{-1}}$. By contrast, weak inflow was present from the boundary layer to 450 hPa near the center of the cyclone, and strong outflow dominated the troposphere on the northern side of the ETC to the north from 29°N (Fig.7a). At the RI stage, the inflow strengthened in the southern side, especially in the boundary layer, with the maximum speed exceeding 12 m $\mathrm{s^{-1}}$ near the center at 0600 UTC 1 August (Fig.7b). Simultaneously, the radial wind exhibited enhanced inflow in the lower troposphere in the northern part of ETC. The inflow extended from the surface to near 700 hPa, with the peak radial wind speed reaching $9\,\mathrm{m\,s^{-1}}$ (Fig.7b). The distribution of the tangential winds shows a quasi-symmetric structure below 500 hPa in the beginning of land-

fall (Fig.7c). Then, the winds strengthened on both sides of Toraji with a maximum speed greater than $27 \, \mathrm{m \, s^{-1}}$ at 500 hPa on the right side and a maximum speed greater than $21 \, \mathrm{m \, s^{-1}}$ in the atmospheric boundary layer on the left side. Thus, the quasi-symmetric structure of the cyclone was destroyed and the storm tilted westwards with height in the vertical direction (Fig.7d).

The vertical cross sections from southwest to northeast through the center of the relative humidity, θ, and wind field are shown in Fig.8. Fig.8a shows that cold air was weak in the middle atmosphere on the southwestern side of the ETC, with the minimum of θ reaching 340 K. By contrast, extensive cold air dominated the middle atmosphere from 850 hPa to 300 hPa on the northeast quadrant of Toraji (Fig.8a). Correspondingly, the ETC exhibited a warm core with one maximum temperature at the boundary and another at the tropopause. The distribution of the relative humidity revealed that wet air existed in the boundary layer on both sides of Toraji (Fig.8a). Wet air

extended from the surface to near 600 hPa in the southwest quadrant. Meanwhile, updraft was predominant on the southwestern side, and weak downdraft existed on the northeastern side of the ETC. As time elapsed, the cyclone re-intensified, and cold and dry air enhanced and extended downstream to the southwest boundary of Toraji (Fig.8b). At the same time, warm and wet air in the boundary and lower troposphere in the northeast quadrant strengthened and extended upward. The wind field exhibited that the northeastern part of the ETC was characterized by weak upward motion because of intense flow from the lower atmosphere (Fig.8b). Correspondingly, the wind field formed a circulation on the vertical section in the lower atmosphere, with the downward motion dominating the troposphere in the southwest quadrant between 28°N and 34°N. The above analysis suggests that the processes of the ET and RI are always accompanied by the presence of cold and dry air (Emanuel *et al.*, 1994; Zhu *et al.*, 2005b).
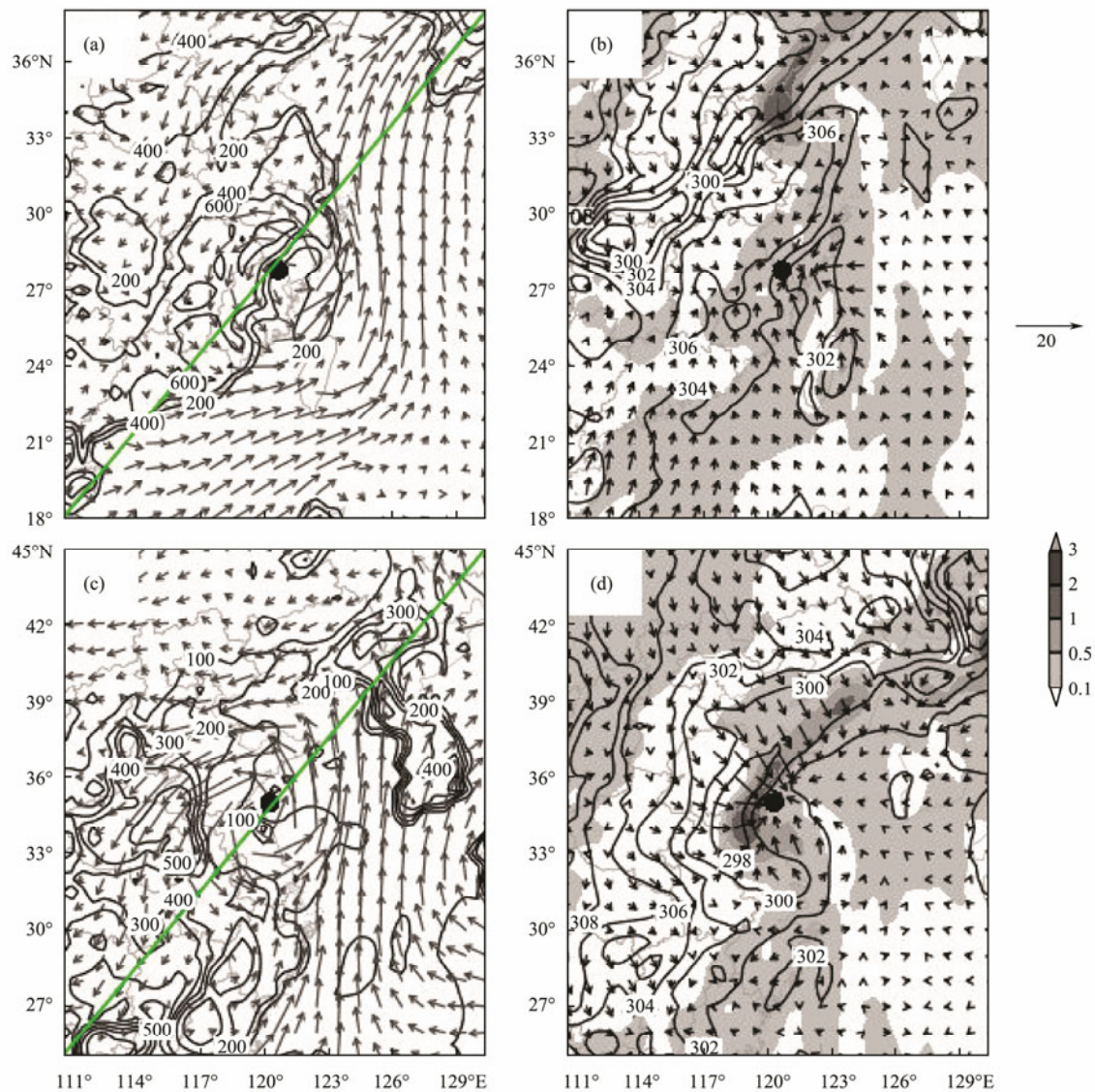
Fig.6 SLHF (contours; $\mathrm{W \, m^{-2}}$) and non-divergent wind (arrows; $\mathrm{m \, s^{-1}}$) at 950 hPa at (a) 0600 UTC 31 July, (c) 0600 UTC 1 August. PV (shaded; PUV), potential temperature (θ, contours; K), and irrotational wind (arrows; $\mathrm{m \, s^{-1}}$) at 950 hPa at the same time are shown in (b), (d). (●: the location of typhoon center).
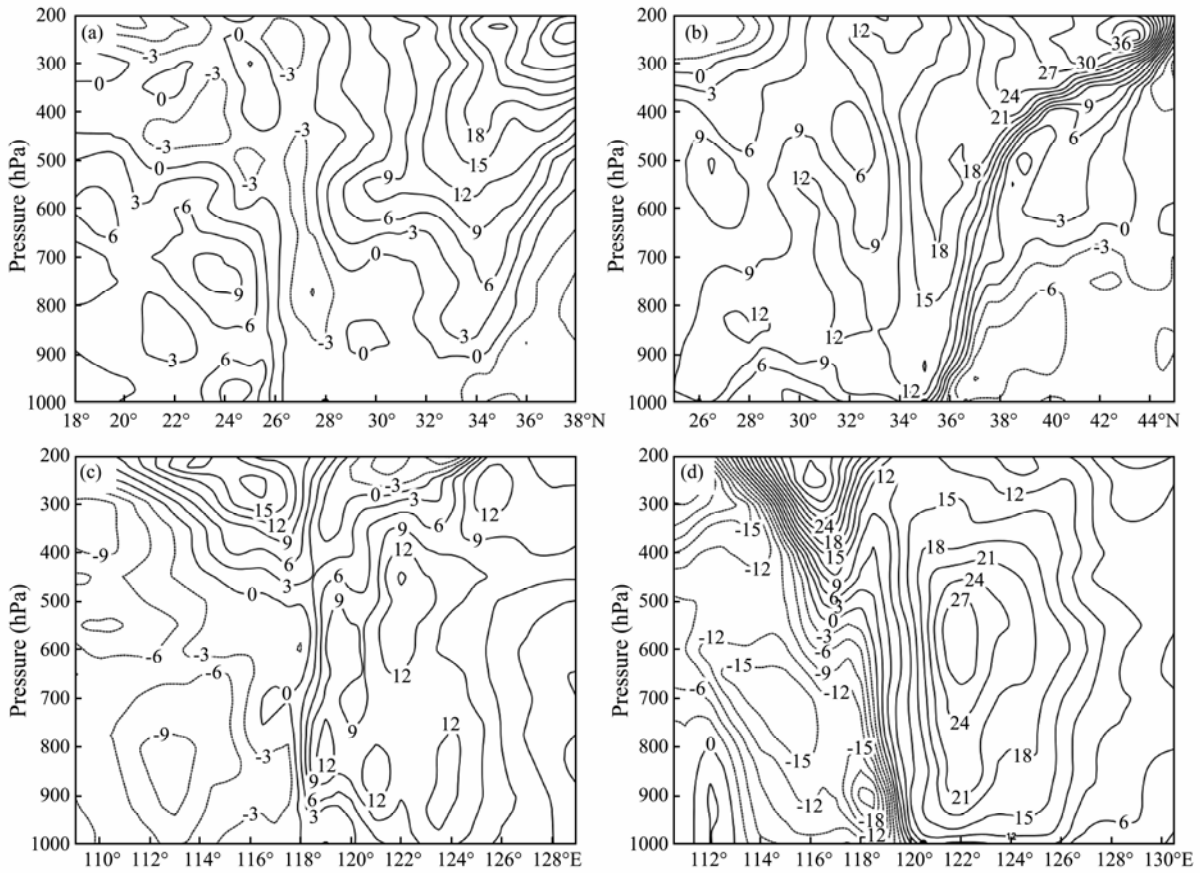
Fig.7 Vertical cross section of radial wind (a and b) and tangential wind (c and d) (contours; m s^{-1}) through the storm center at (a) and (c) 0600 UTC 31 July (b) and (d) 0600 UTC 1 August. (●: the location of typhoon center).
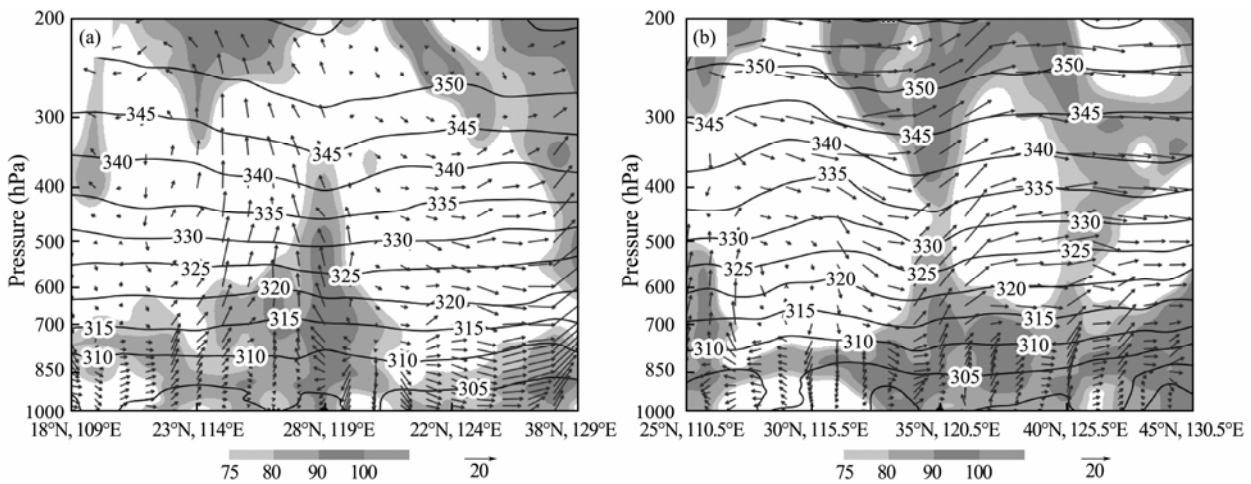
Fig.8 Vertical cross section of relative humidity (shaded; ≥75), potential temperature (θ, contours; K), and wind field (wind vectors are parallel to the cross section with ω multiplied by a factor of 30; m s^{-1}) at (a) 0600 UTC 31 July and (b) 0600 UTC 1 August. (a) and (b) correspond to the green baseline cases shown in Figs.6a and 6c, respectively (●: the location of typhoon center).

4.3 Frontogenesis

In previous studies, the ET process was considered an interaction between a cyclone and a baroclinic zone (Doswell, 1985), accompanied by developing frontogenesis. Sekioka (1956a, b, 1970) and Matano and Sekioka (1971) showed that a TC does not transform into an EC and reintensify, but decays and dissipates unless it encounters an invading cold front. Harr and Elsberry (2000) studied the frontogenesis of cyclones interacting with a preexisting trough to the northwest and northeast and described ET of TC.

We described the horizontal and vertical structure of the wind field, equivalent potential temperature, and relative humidity. The feature of their distribution (Figs.3 and 8) indicates that the fronts develop in the northeast and

southwest quadrants of the storm. To express the cold air intrusion and the physical process caused by the interaction between the cyclone and the baroclinic zone (mid-latitude systems), we calculate the three-dimensional scalar frontogenesis parameter (SFP) (Harr and Elsberry, 2000) as follows:

$$F_n = -|\nabla_h \theta|^{-1} \left[\frac{\partial \theta}{\partial x} \left(-\frac{\partial u}{\partial x} \frac{\partial \theta}{\partial x} - \frac{\partial v}{\partial x} \frac{\partial \theta}{\partial y} \right) + \right.$$

$$\left. \frac{\partial \theta}{\partial y} \left(-\frac{\partial u}{\partial y} \frac{\partial \theta}{\partial x} - \frac{\partial v}{\partial y} \frac{\partial \theta}{\partial y} \right) + \frac{\partial \theta}{\partial p} \left(-\frac{\partial \omega}{\partial x} \frac{\partial \theta}{\partial x} - \frac{\partial \omega}{\partial y} \frac{\partial \theta}{\partial y} \right) \right], (1)$$

where θ is the potential temperature, and ω is the vertical motion in the pressure coordinates. The first term on the right-hand side of Eq. (1) is the divergence of frontogenesis (denoted by F_n-div), the second term is the deformation of frontogenesis (denoted by F_n-def), and the third term is the tilt of frontogenesis (denoted by F_n-tilt). Positive (negative) $-F_n$ corresponds to the frontogenesis (fron-

tolysis).

The horizontal and dynamic structure of a cyclone can be depicted by geopotential height, divergence, vertical velocity, and SFP (Figs.9 and 10). Results reveal that the tilting term (F_n-tilt) associated with vertical motion dominates the positive frontogenesis surrounding the ETC center (Figs.9d and 10d), which is consistent with Kofron *et al.* (2010). This result is different from that of a previous study on the early ET stage (Han *et al.*, 2005). By contrast, the contributions of F_n-div and F_n-def are trivial. At 0600 UTC 31 July, the horizontal distribution of scalar frontogenesis (Fig.9a) and the evolution of potential temperature (Fig.9c) indicated a cold frontogenesis in the southwest quadrant of Toraji. Weak scalar frontolysis occurred north of the center in the warm frontal region (not shown). Fig.9b shows a convergence band in the northern–western–southern side of Toraji, as shown by satellite images (not shown). The contribution of convergence and divergence to the frontogenesis is negligible surrounding the ETC except that on the northern side, as
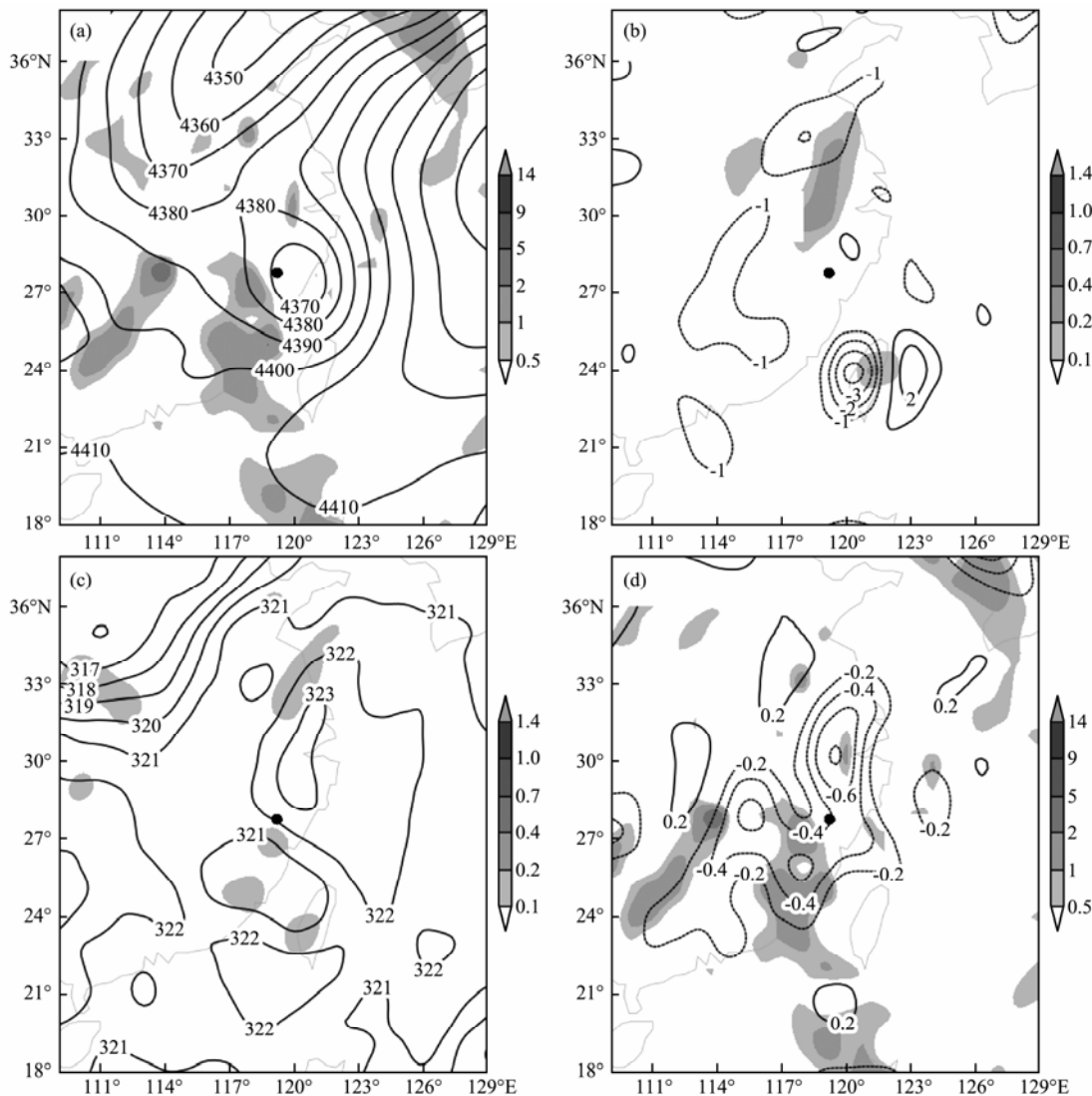
Fig.9 600-hPa SFP and its components (shaded; $\mathrm{K}\,(100\,\mathrm{km})^{-1}\,(3\,\mathrm{h})^{-1}$): (a) $-F_n$ and geopotential height (contours; gpm), (b) $-F_n$-div and divergence (contours; $10^{-5}\,\mathrm{s}^{-1}$), (c) $-F_n$-def and potential temperature (contours; K), and (d) $-F_n$-til and vertical velocity (contours; $\mathrm{Pa}\,\mathrm{s}^{-1}$) at 0600 UTC 31 July. The cyclone centers are marked '•'.
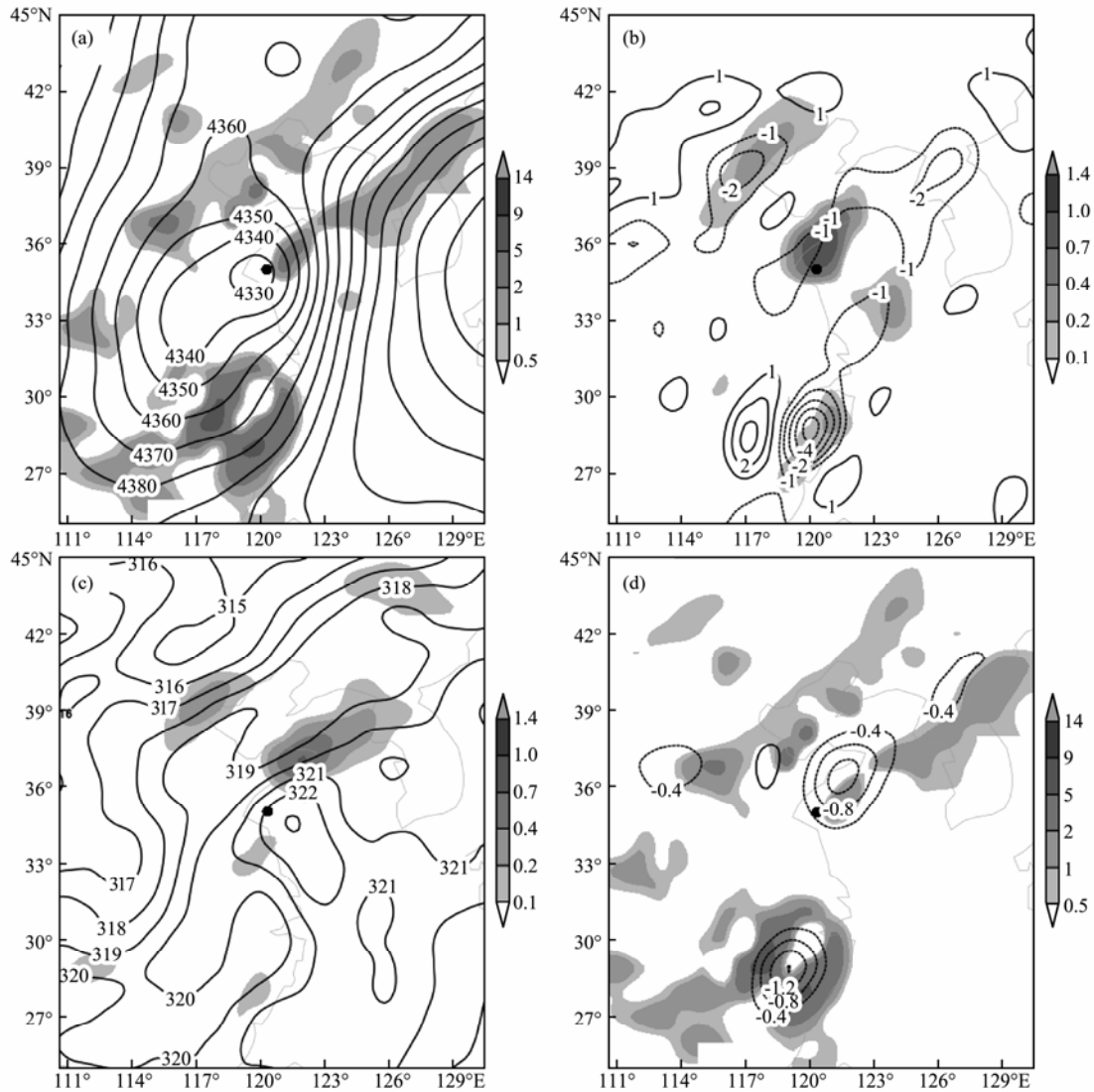
Fig.10 Same as Fig.9, but for 0600 UTC 1 August.

well as the term of deformation (Fig.9c). At the same time, the horizontal distribution of vertical velocity is similar to the distribution of divergence, but the contribution of F_n-tilt to frontogenesis dominates the southwest quadrant.

At 0600 UTC 1 August, when the ETC re-intensified, the $-F_n$ amplified in the southwest quadrant and extended eastward (Fig.10a). However, the distance of the frontogenesis from the center increased, which was primarily provided by the F_n-tilt (Fig.10d). Simultaneously, positive $-F_n$ occurred in the northeast quadrant of the ETC, where the warm frontal features are indicated by a strong temperature gradient (Fig.10c) and wind field (Figs.3 and 8b), among others. Correspondingly, another positive $-F_n$ is produced in the northwest quadrant associated with the cold frontal zone. A comparison between the details of Figs.10b and 9b shows that divergence replaced convergence in the southwest quadrant, and the contribution of convergence (F_n-div) to the frontogenesis is obvious on the northern side of the ETC (Fig.10b), although a portion of F_n-div is counteracted by frontolysis of F_n-til near the center. By contrast, the contribution of F_n-tilt for fronto-

genesis takes place at the northwest and northeast quadrants, which are associated with a strong temperature gradient (Fig.10c).

4.4 Kinetic Energy Budget

Although kinetic energy converted from baroclinic potential energy due to cold air intrusion is trivial in the total energy balance, it is important for persistence and RI when a typhoon moves to the mid-latitude zone (Thorncroft and Jones, 2000; Hart and Evans, 2002). The kinetic energy budget equation in pressure coordinates (Ward and Smith, 1976) is as follows:

$$\frac{\partial K}{\partial t} = \frac{1}{gA}\left\{\iiint -\vec{V}\cdot\nabla\phi\,\mathrm{d}\sigma\mathrm{d}p + \iint -\nabla\cdot\vec{V}k\mathrm{d}\sigma\mathrm{d}p + \right.$$

$$\left. \iint -\frac{\partial k\omega}{\partial p}\mathrm{d}\sigma\mathrm{d}p\right\} + R, \qquad (2)$$

where $\vec{V}(=\vec{V}_D + \vec{V}_R)$ is the wind vector and can be presented by divergent ($\vec{V}_D$) and rotational ($\vec{V}_R$) wind components; $k = \vec{V}\cdot\vec{V}/2$ is the kinetic energy per unit mass,

$K(=\dfrac{1}{gA}\iint k \mathrm{d}\sigma \mathrm{d}p)$ is the kinetic energy of atmospheric volume; $\Phi=gZ$, g and Z are the gravity acceleration and the geopotential height, respectively; A is the computational area; and ω is the same as in Eq. (1); the other symbols are common meteorology symbols. The left side of Eq. (2) is the local variation of kinetic energy (GKT). The first term on the right side of Eq. (2) is the kinetic energy generation (GKE) and can be divided into divergent and rotational kinetic energy generations (GKD and GKR), which is the primary kinetic energy. GKD is closely related to atmospheric baroclinicity, and GKR can stand for atmospheric barotropy; both will be described. The second term is the horizontal divergence of kinetic energy (HFC). The third term is the vertical divergence of kinetic energy (VFC), and the fourth term is the energy in the residual (R). In this study, GFRS data are employed with a span of 0.5°, and the computational area is a 10°× 10° square with 28 levels from the surface to 200 hPa in a vertical orientation with its center representing that of the typhoon.

The circulation of the cyclone shows that the wind enhances and transforms from an oval to a quasi-symmetrical structure in the RI stage (Figs.5 and 7), which implies the strengthening of kinetic energy. Fig.11 shows the temporal variation of regionally averaged kinetic energy (KE), divergent kinetic energy (KD), and rotational kinetic energy (KR). KE values reflect these variations, exhibiting a decrease during the first 12 h with an invariable MSLP of 1000 hPa (Fig.1b). Afterwards, KE generally increases throughout the RI stage until 1800 UTC 1 August. Thus, the cause of RI can be explained as the variating kinetic energy budget because of the close coincident trend of KE and MSLP. The variation of KD and KR is similar to that of KE during the entire calculation period, whereas 83.7% of KE can be explained as KR (Fig.11a). KR is the major part of KE due to the quasi-geostrophy of atmospheric motion, which is consistent with Chen *et al.* (1978). The cross section of KE (Fig.11b) reveals a homologous vertical pattern and the increasing KE as a positive column total. During the calculation period, KE increases in the upper troposphere, but energy content decreases in the initial 12 h and then increases near the surface (Fig.11b). A major increase near 850 hPa occurs when the cyclone moves to the Bohai Sea 6 h after intense peaking at 1800 UTC 1 August. The distribution of KR (Fig.11c) in the vertical cross section is similar to that of KE (Fig.11b). KD evidently increases in the upper troposphere and near the surface throughout the period, although the KD values are trivial relative to the KR val-
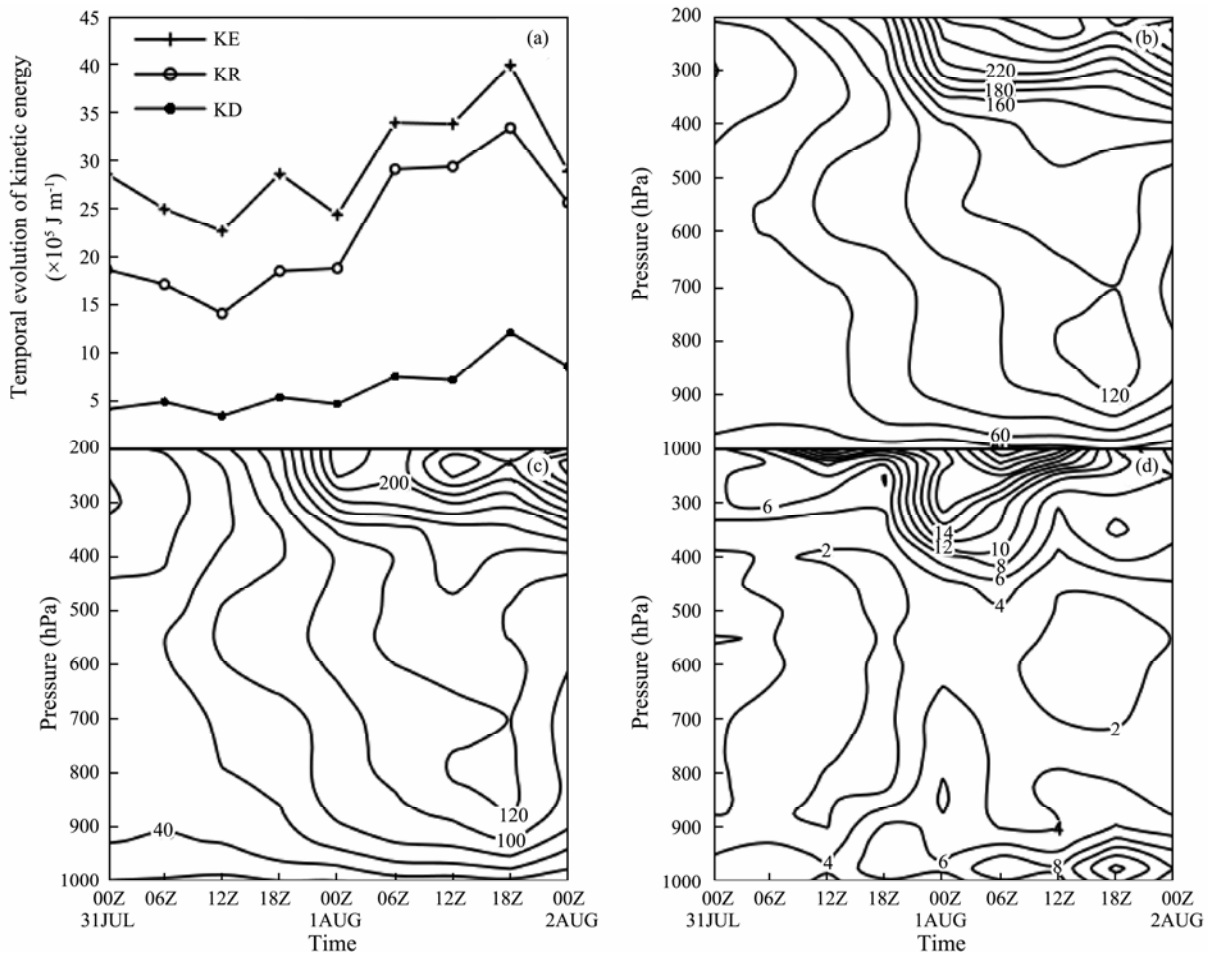
Fig.11 (a) Temporal evolution of kinetic energy of an atmospheric volume of KE (vector winds), KR (rotational winds), and KD (divergent winds). Pressure-time cross sections of area-averaged (b) KE, (c) KR, and (d) KD. The region is a 10°×10° square with its center representing that of the typhoon, the same as in Figs.12 and 14.

ues (Fig.11d). In the upper atmosphere, a maximum value of $26 \, \mathrm{J \, kg^{-1}}$ occurs near 200 hPa 6 h before intense peaking at 0600 UTC 1 August and KD begins to decrease when the ETC peaks again (Fig.11d).

Corresponding to the strengthening of KE, KR, and KD in the upper atmosphere, the relative position between the cyclone in transition and the upper jet is important (Bosart and Atallah, 2000). When the storm moved to the upper jet entrancing area, the pumping of the high-altitude divergence enhanced irrotational outflow and low-level cyclone convergence (Fig.4). In the lower atmosphere, except for the contribution of LJ (Fig.3), cold air

intrusion enhanced the baroclinic storm and convergent circulation in the northeastern and southwestern sides of the system, which is associated with the increased equivalent potential temperature gradient (Fig.6d).

Fig.12 shows the pressure-time cross sections of the area-averaged terms of Eq. (2). In the initial 12 h, the GKT values were negative in the lower troposphere (below 600 hPa) because of surface friction (Fig.12a). Positive GKT values dominated the troposphere with a peak ($2 \, \mathrm{W \, m^{-2}}$) near 250 hPa at 0600 UTC 1 August at the RI stage associated with the enhancement of circulation. The positive GKE values associated with wind crossing from higher to
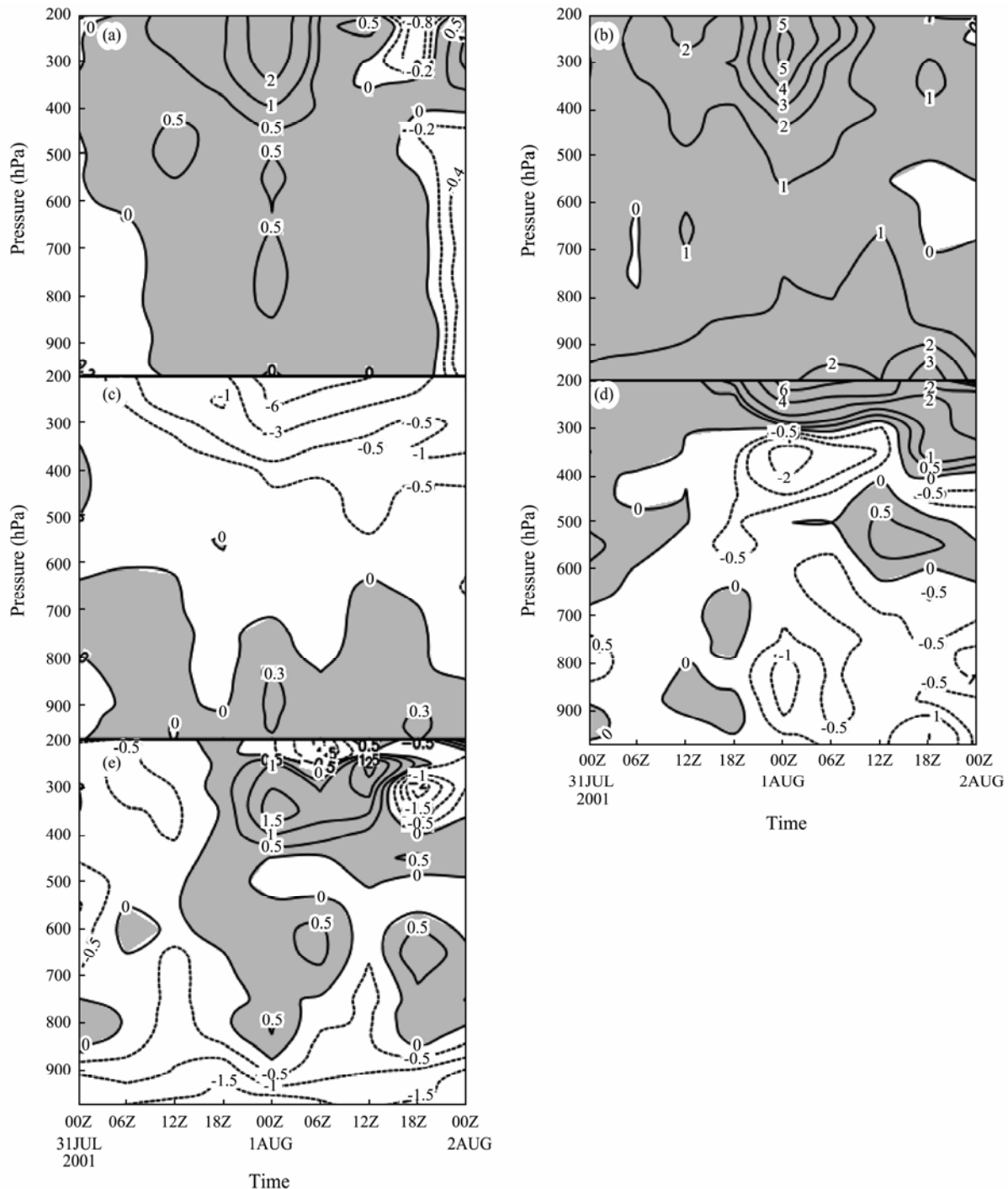
Fig.12 Pressure-time cross sections of area-averaged (a) GKT, (b) GKE, (c) HFC, (d) VFC, and (e) R (Shaded: positive values; $\mathrm{W \, m^{-2}}$).

lower heights (Fig.12b) were located in the upper (above 400) and the lower troposphere (below 850 hPa). In the upper atmosphere, GKE was enhanced with a maximum positive value of 5 W m^{-2} near 250 hPa at 0300 UTC 1 August, corresponding to the peak values of GKT. The GKE values in the lower troposphere increased with the northward movement of the ETC, with the peak value exceeding 3 W m^{-2} near the surface at 1800 UTC 1 August (Fig.12b). The distribution of HFC indicated the KE transition between the cyclone and the surrounding atmosphere in the horizontal direction. A positive HFC existed in the boundary layer and the lower troposphere with a smaller magnitude (Fig.12c), which demonstrated the energy conversion from the surrounding region to the storm. By contrast, the largest contributor, which was the negative values in the upper levels, indicated that KE conveyed from the volume to the surrounding region (Fig.12c), which might be attributed to the outflow from the cyclone (Fig.4). For VFC associated with energy conveyed downward, the primary positive values were concentrated in the upper atmosphere, and the negative values were dominant in the middle and lower atmosphere (Fig.12d). The positive values trended downward to the boundary layer before 1800 UTC 31 July and induced the conservation and development of the cyclone, which was similar to the B-type EC. Afterwards, the positive area experienced a complex period, contracting upward and intensifying with a maximum value of 6 W m^{-2} at 0000 UTC 1 August, and then extending downward and decreasing (Fig.12d). The negative values extended from the surface to near 300 hPa at 2100 UTC 31 July and stayed below 600 hPa, which indicated that the KE conveyed upward in the vertical direction (Fig.12d). The distributions of R showed that the negative values of KE primarily dominated the lower atmosphere (Fig.12e).

The distribution of geopotential height (Figs.6, 9 and 10) shows that the temperature gradient is weak in the maintenance stage after Toraji made landfall. The temperature gradient enhanced in the northeast and northwest quadrants when Toraji merged with another cyclone over Shandong Peninsula in the lower atmosphere. By contrast, the distribution of VFC (Fig.12d) indicates that the positive values trended downward to the boundary layer before 1800 UTC 31 July and induced the conservation and development of the cyclone, and then the KE conveyed upward in the vertical direction as the cyclone intensified, which corresponds to the distribution of the E-P fluxes with vertically downward propagation at 0600 UTC 31 July (Fig.13a) and upward-conveyor momentum at 0600 UTC 1 August (Fig.13b). The transmission of the E-P fluxes is particularly evident in the middle and lower atmosphere. Thus, the RI of Toraji was a complex pattern that contained the development of A- and B-type ECs. However, this pattern is different from that of Cyclone Winner (1997), which was studied by Zhu *et al.* (2005a).

The above analysis shows that the strengthening of KE was dominated by GKE and VFC in the upper atmosphere (Figs.12b and 12d) and by GKE in the lower atmosphere (Fig.12b). By contrast, the contribution of GKE and VFC were partially offset by HFC in the upper troposphere. To further determine the detailed impact of GKE, the temporal variation of GKR and GKD is shown in Fig.14. The GKR values increased as the decaying TC re-intensified into an EC from 0000 UTC 31 July to 0900 UTC 1 August and then became negative in the upper troposphere (Fig.14a). Meanwhile, low positive and negative GKR values were found below 750 hPa. The pressure-time cross section of GKD in the KE budget throughout the ET and RI of Toraji (Fig.14b) indicates that the positive GKD values occurred in the upper troposphere with a maximum value of 3 W m^{-2} at 0300 UTC 1 August, and the peak value near the surface exceeded 3 W m^{-2} at 1800 UTC 1 August. Analysis (Figs.12b, 14a, and 14b) suggests that GKE was supplied by GKR and GKD during RI in the upper troposphere, which was attributed to the effect of upper trough and jet. By contrast, GKD was the primary term in the generation of KE in the lower levels. Simultaneously, temporal evolution of the terms of atmosphere volume in the KE budget (not shown) showed that GKE was a significant source of energy.
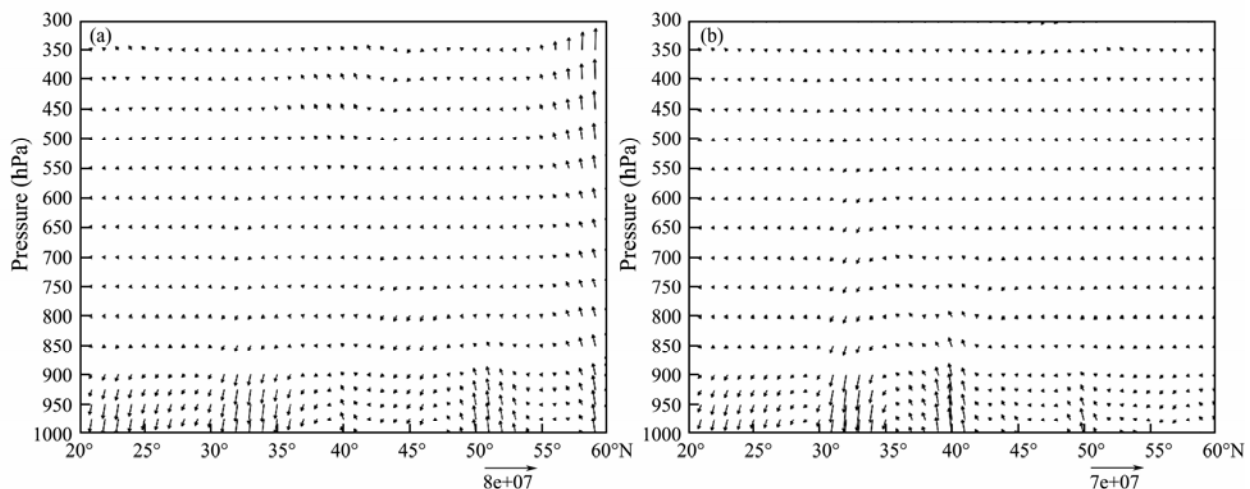
Fig.13 Vertical cross section of the E-P fluxes through the storm center (vectors; unit: m^2 s^{-2}). The time is the same as in Figs.8a and 8b.
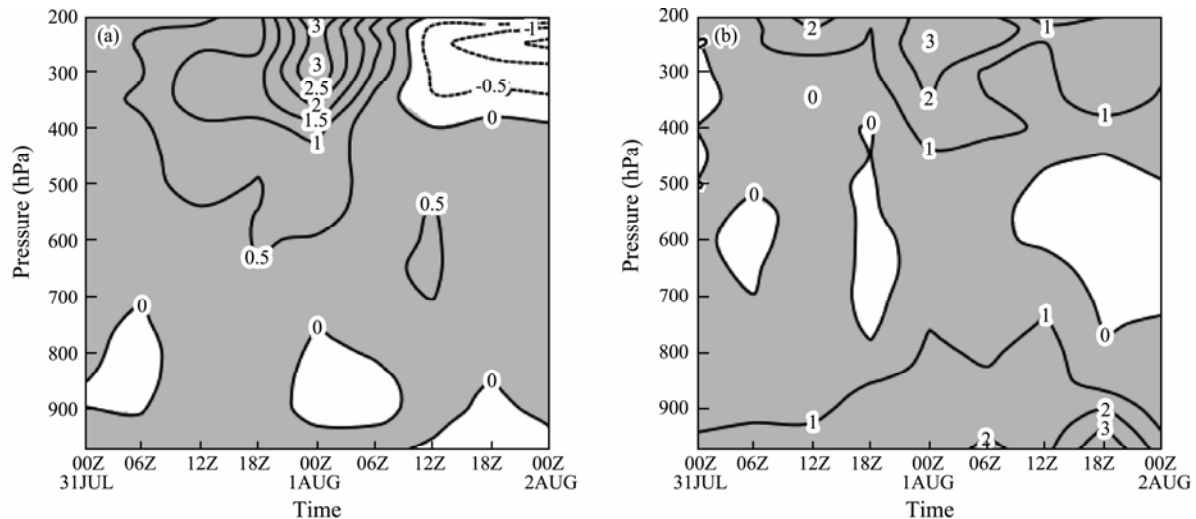
Fig.14 Pressure-time cross sections of area-averaged (a) GKR, (b) GKD (Shaded: positive values; $\mathrm{W\,m^{-2}}$).

Therefore, GKD at the lower levels could be considered as the primary factor that resulted in the RI of Toraji. Further research demonstrated that GKD was closely related to cold air intrusion through a comparison among the distribution of GKD (not shown), irrotational wind, and potential temperature (Fig.6). The above analyses show that the interaction between the EC and the mid-latitude synoptic system plays an important role in the RI stage of Toraji. The analyses of Palmen (1958) and Harr and Hogan (2000) indicate that the coupling between the decaying TC and the mid-latitude circulation contributes to the conversion of available potential energy into KE *via* solenoidal circulation, where cold air sinks in the thermal trough upstream of the decaying TC and warm air rises in the downstream thermal ridge.

5 Discussion and Summary

A decaying TC (Toraji) undergoes an RI period as an intense EC during ET. To determine the structural characteristics and mechanisms of such an occurrence, data from JMA, GRSR, and GOES-9 are employed. The analysis successfully reveals the path, intensity change, and structural evolutions of Toraji. The results are summarized below.

In the upper atmosphere, the existence of the upper jet is important to the development of the TC. When Toraji moved to the area of the upper jet entrance, where high-altitude outflow exists, the pumping of the divergence would enhance vertical motion and low-level cyclone convergence. Simultaneously, the existence of LJ further enhances the vertical motion when the ETC is located at the left side of LJ. At the transformation stage, TR1 moves the low-level ETC eastward with a warm core, which is similar to the development of a B-type EC. By contrast, cold air intrusion conveyed by TR1 can result in increased baroclinic instability and provide favorable conditions for the RI.

The evolution of the circulation of the ETC shows that both the rotational wind and the divergent wind strengthen on both sides of the best track with the magnitude of the wind reinforcing on the left side at the RI stage, accompanied with shrunk MSW in the lower atmosphere. In addition, the wind field exhibits a quasi-symmetric pattern evolving from an oval to a ring. By contrast, a decreasing SLHF is located at the inner core of Toraji and an increasing SLHF enlarges near the surface from the center in the northeast and southwest quadrants of the ETC. The potential temperature gradient increases in the northwestern side of the center because of the cold air intrusion, which is associated with the strengthening of PV and the divergent wind in the lower atmosphere. Corresponding to the horizontal distribution of the wind field and θ, the cold frontal features are indicated with cold air and a downward motion dominating the troposphere in the southwest quadrant in contrast to the warm frontal features in the northeast quadrant.

The cold air intrusion enhanced the baroclinicity of the atmosphere and the formation of fronts. The results demonstrate that the F_n-tilt associated with vertical motion dominates positive frontogenesis in the southwest and northeast quadrants, which correspond to cold frontal and warm frontal structures, respectively. At the RI stage, the conversion from baroclinic potential energy to KE enhanced in the upper and lower troposphere because of cold intrusion and frontogenesis. The pressure–time cross sections of the primary terms in the KE budget show that the contribution of GKE is a significant component when the contribution of VFC is partially offset by HFC. Thereafter, this research further indicates that GKD plays an important role in the lower troposphere during the development period, which is associated with the baroclinicity of the atmosphere. Meanwhile, the vertical distribution of VFC demonstrates that RI of Toraji also possesses a typical feature similar to the development of an A-type EC by upward converting energy.

Therefore, the RI of Toraji is a complex pattern that contained a similar development as A- and B-type ECs, which is different from the pattern of Winner (1997) in a previous study (Zhu *et al.*, 2005a). In the early RI stage,

ETC (Toraji) persisted as a result of energy conveying downward. Afterwards, Toraji strengthened because of the superposition of two cyclones over Shandong Peninsula when the ETC moved northward. Meanwhile, due to cold air intrusion, frontogenesis developed in the northeastward and southwestward quadrants. The result of frontogenesis forced strong convergence and vertical secondary circulation. Then, baroclinic potential energy was converted into KE, which also increased the ETC and transported energy upward. Thus, the enhanced upper divergence further gave rise to lower atmosphere convergence, which was a positive feedback for ETC.

ET is a complex evolutionary process that involves interactions over a variety of horizontal and vertical scales (Jones *et al.*, 2003). In this study, the RI stage of Toraji is emphasized, and its structural characteristics and mechanisms are concluded. However, some questions remain unanswered, such as the temporal evolution of the frontogenesis in different quadrants.

Acknowledgements

References

Bosart, L. F., and Atallah, E. H., 2000. Extratropical transition: Large-scale aspects. *24th Conference on Hurricane and Tropical Meteorology*. Fort Lauderdale, Florida, 284-285.

Chen, H., and Pan, W., 2010. Targeting studies for the extratropical transition of hurricane Fabian: Signal propagation, the interaction between Fabian and midlatitude flow, and an observation strategy. *Monthly Weather Review*, **138** (8): 3224-3242.

Chen, L. S., 2000. An overview on the impact of interaction between low-mid latitude circulation on rainfall and tropical cyclone behavior. *24th Conference on Hurricanes and Tropical Meteorology*. Fort Lauderdale, Florida, 63-65.

Chen, L. S., and Ding, Y. H., 1979. *An Introduction to the Western Pacific Typhoon*. Science Press, Beijing, 491pp (in Chinese).

Chen, T. C., Alpert, J. C., and Schlatte, T. W., 1978. The effects of divergent and nondivergent winds on the kinetic energy budget of a mid-latitude cyclone: A case study. *Monthly Weather Review*, **106** (4): 458-468.

Cordeira, J. M., and Bosart, L. F., 2011. Cyclone interactions and evolutions during the　perfect storms　of late October and early November 1991. *Monthly Weather Review*, **139** (6): 1683-1707.

Dare, R. A., and Davidson, N. E., 2004. Characteristics of tropical cyclones in the Australian region. *Monthly Weather Review*, **132** (12): 3049-3065.

Demirci, O., Tyo, J. S., and Ritchie, E. A., 2007. Spatial and spatiotemporal projection pursuit techniques to predict the extratropical transition of tropical cyclones. *IEEE Transactions on Geoscience and Remote Sensing*, **45** (2): 418-425.

DiMego, G. J., and Bosart, L. F., 1982a. The transformation of tropical storm Agnes into an extratropical cyclone. Part I: The observed fields and vertical motion computations. *Monthly Weather Review*, **110** (5): 385-411.

DiMego, G. J., and Bosart, L. F., 1982b. The transformation of tropical storm Agnes into an extratropical cyclone. Part II: Moisture, vorticity and kinetic energy budgets. *Monthly Weather Review*, **110** (5): 412-433.

Doswell, C. A., 1985. A kinematic analysis of frontogenesis associated with a nondivergent vortex−Reply. *Journal of Atmospheric Sciences*, **42** (19): 2076-2079.

Emanuel, K. A., Neelin, J. D., and Bretherton, C. S., 1994. On large-scale circulations in a nearly inviscid atmosphere. *Quarterly Journal of Royal Meteorological Society*, **120**: 1111-1143.

Evans, C., and Hart, R. E., 2008. Analysis of the winds field evolution associated with the extratropical transition of Bonnie (1998). *Monthly Weather Review*, **136** (6): 2047-2065.

Evans, J. L., and Prater-Mayes, B. E., 2004. Factors affecting the post transition intensification of hurricane Irene (1999). *Monthly Weather Review*, **132** (6): 1355-1368.

Foley, G. R., and Hanstrum, B. N., 1994. The capture of tropical cyclones by cold fronts off the west coast of Australia. *Weather & Forecasting*, **9** (4): 577-592.

Han, G. R., He, J. H., and Fan, Y. F., 2005. The transfiguration frontogenesis analyses on 0108 landfall typhoon extratropical transition and heavy rain structure. *Acta Meteorologica Sinica*, **63** (4): 468-476 (in Chinese with English abstract).

Harr, P. A., and Dea, J. M., 2009. Downstream development associated with the extratropical transition of tropical cyclones over the western North Pacific. *Monthly Weather Review*, **137** (4): 1295-1319.

Harr, P. A., and Elsberry, R. L., 2000. Extratropical transition of tropical cyclones over the western North Pacific. Part I: Evolution of structural characteristics during the transition process. *Monthly Weather Review*, **128** (8): 2613-2633.

Harr, P. A., and Hogan, T. F., 2000. Extratropical transition of tropical cyclones over the western North Pacific. Part II: The impact of midlatitude circulation characteristics. *Monthly Weather Review*, **128** (8): 2634-2653.

Hart, R. E., and Evans, J. L., 2001. A climatology of the extratropical transition of Atlantic tropical cyclones. *Journal of Climate*, **14** (4): 546-564.

Hart, R. E., and Evans, J. L., 2002. Extratropical transition: One trajectory though cyclone phase space. *25th Conference on Hurricanes and Tropical Meteorology*. American Meteorological Society, San Diego, CA, 539-540.

Jones, S. C., 1995. The evolution of vortices in vertical shear I: Initially barotropic vortices. *Quarterly Journal of the Royal Meteorological Society*, **121** (524): 821-851.

Jones, S. C., Harr, P. A., Abraham, J., Bosart, L. F., Bowyer, P. J., Evans, J. L., Hanley, D. E., Hanstrum, B. N., Hart, R. E., Lalaurette, F., Sinclair, M. R., Smith, R. K., and Thorncroft, C., 2003. The extratropical transition of tropical cyclones: Forecast challenges, current understanding, and future directions. *Weather & Forecasting*, **18** (6): 1052-1092.

Kitabatake, N., 2008. Extratropical transition of tropical cyclones in the western North Pacific: Their frontal evolution. *Monthly Weather Review*, **136** (6): 2066-2090.

Klein, P. M., Harr, P. A., and Elsberry, R. L., 2000. Extratropical transition of western North Pacific tropical cyclones: An overview and conceptual model of the transformation stage. *Weather & Forecasting*, **15** (4): 373-395.

Klein, P. M., Harr, P. A., and Elsberry, R. L., 2002. Extratropi-

cal transition of western North Pacific tropical cyclones: Mid-latitude and tropical cyclone contributions to re-intensification. *Monthly Weather Review*, **130** (9): 2240-2259.

Kofron, D. E., Ritchie, E. A., and Tyo, J. S., 2010. Determination of a consistent time for the extratropical transition of tropical cyclones. Part I: Examination of existing methods for finding 'ET time'. *Monthly Weather Review*, **138** (12): 4328-4343.

Li, Q. B., Huang, M. Z., and Lin, Y., 2004. The analysis of re-intensification of typhoon Toraji. *Transactions of Oceanology*, **23** (6): 16-20 (in Chinese with English abstract).

Loridan, T., Scherer, E., Dixon, M., Bellone, E., and Khare, S., 2014. Cyclone winds field asymmetries during extratropical transition in the Western North Pacific. *Journal of Applied Meteorology and Climatology*, **53** (2): 421-428.

Matano, H., and Sekioka, M., 1971. On the synoptic structure of typhoon Cora 1969 as the compound system of tropical and extratropical cyclone. *Journal of Meteorological Society of Japan*, **49**: 282-294.

McTaggart-Cowan, R. J., 2002. Influence of the downstream state on extratropical transition hurricane Earl (1998) case study. *25th Conference on Hurricanes and Tropical Meteorology*. American Meteor Society, San Diego, California, 543544.

Merrill, R. T., 1993. Tropical cyclone structure. Global Guide to Tropical Cyclone Forecasting, WMO/TD-560, Rep. TCP-31, World Meteorological Organization, Geneva, Switzerland, 2.1-2.60.

Onogi, K., Tsutsui, J., Koide, H., Samamoto, M., Kobayashi, S., Hatsushika, H., Matsumoto, T., Yamazaki, N., Kamahori, H., Takahashi, K., Kadokura, S., Wada, K., Kato, K., Oyama, R., Ose, T., Mannoji, N., and Taira, R., 2007. The JRA-25 Reanalysis. *Journal of Meteorological Society of Japan*, **85** (3): 369-432.

Palmen, E., 1958. Vertical circulation and release of kinetic energy during the development of hurricane Hazel into an extratropical storm. *Tellus*, **10** (1): 1-23.

Petterssen, S., and Smebye, S. J., 1971. On the development of extratropical cyclones. *Quarterly Journal of Royal Meteorological Society*, **97**: 457-482.

Quinting, J. F., Bell, M. M., Harr, P. A., and Jones, S. C., 2014. Structural characteristics of T-PARC typhoon Sinlaku during its extratropical transition. *Monthly Weather Review*, **142** (5): 1945-1961.

Ritchie, E. A., and Elsberry, R. L., 2001. Simulations of the transformation stage of the extratropical transition of tropical cyclones. *Monthly Weather Review*, **129** (6): 1462-1480.

Sekioka, M., 1956a. A hypothesis on complex of tropical and extratropical cyclones for typhoon in the middle latitudes. I. Synoptic structure of typhoon Marie over the Japan Sea. *Journal of Meteorological Society of Japan*, **34**: 276-287.

Sekioka, M., 1956b. A hypothesis on complex of tropical and extratropical cyclones for typhoon in the middle latitudes. II. Synoptic structure of typhoons Louise, Kezia and Jane passing over the Japan Sea. *Journal of Meteorological Society of Japan*, **34**: 336-345.

Sekioka, M., 1970. On the behaviour of cloud pattern as seen on satellite photographs in the transformation of a typhoon into an extratropical cyclone. *Journal of Meteorological Society of Japan*, **48**: 224-233.

Sinclair, M. R., 2002. Extratropical transition of southwest Pacific tropical cyclones. Part I: Climatology and mean structure changes. *Monthly Weather Review*, **130** (3): 590-609.

Thorncroft, C. D., and Jones, S. C., 2000.The extratropical transitions of Hurricane Felix and Iris. *Monthly Weather Review*, **128** (4): 947-972.

Vancas, M., 2006. The extratropical transition of tropical storm Banyan. Master thesis. Department of Meteorology, Naval Postgraduate School, Monterey, CA.

Wang, C. M., Wu, R. S., and Wang, Y., 2002. Interaction of diabatic frontogenesis and moisture process in cold-frontal rain-band. *Advances in Atmospheric Sciences*, **19** (3): 544-561.

Ward, J. H., and Smith, P. J., 1976. A kinetic energy budget over North America during a period of short synoptic wave development. *Monthly Weather Review*, **104** (7): 836-848.

Zhu, P. J., Zheng, Y. G., and Tao, Z. Y., 2005a. Kinetic energy budget of typhoon during extratropical transition. *Journal of the Beijing University*, **22** (5): 93-103 (in Chinese with English abstract).

Zhu, P. J., Zheng, Y. G., Zhang, C. X., and Tao, Z. Y., 2005b. A study of the extratropical transformation of typhoon Winnie (1997). *Advances in Atmospheric Sciences*, **41** (1): 730-740.

(Edited by Xie Jun)